Materials Today Bio 28 (2024) 101235

Contents lists available at ScienceDirect

Materials Today Bio

journal homepage: www.journals.elsevier.com/materials-today-bio

Decellularized adipose-derived matrix from Superficial layers of abdominal adipose tissue exhibits superior capacity of adipogenesis compared to deep layers

Xiaomu Ma [1], Qiang Yue [1], Su Fu, Chunjun Liu [2,**], Jie Luan [2,*]

Plastic Surgery Hospital, Peking Union Medical College, Chinese Academy of Medical Sciences, Beijing, 10014, China

ARTICLE INFO

Keywords:
Extracellular matrix
Bioscaffold
Adipose tissue
Superficial subcutaneous fat
Deep subcutaneous fat
Fat regeneration

ABSTRACT

The adipogenic property of decellularized adipose-derived matrix (DAM) varies widely across reports, making it difficult to make a horizontal comparison between reports and posing challenges for the stable clinical translation of DAM. It is possibly due to differences in donor characteristics, but the exact relationship remains unclear. Despite extensive research on the differences between superficial and deep layers of abdominal subcutaneous fat, a main donor of DAM, little is known about their extracellular matrix (ECM) which is promising in regenerative medicine. In this study, we first confirmed the distinct compositional profiles and adipogenic potential between superficial and deep DAM (S-DAM and D-DAM). Both in vitro and in vivo assays confirmed superior adipogenic induction potential in S-DAM over D-DAM. Total amounts of ECM proteins like collagen and laminin were similar, however, the predominant types differed, with collagen I dominating S-DAM and collagen XIV prevailing in D-DAM. S-DAM was enriched with mitochondrial and immunological proteins, whereas D-DAM featured more neuronal, vascular, muscular, and endocrine-related proteins. More proteins involved in mRNA processing were found in D-DAM, with Protein-Protein Interaction (PPI) analysis revealing HNRNPA2B1, HNRNPA1, and HNRNPC as the most tightly interacting members. These findings not only deepen our comprehension of the structural and functional heterogeneity of adipose tissues but also become one of the reason for the large variability between batches of DAM products, providing guidance for constructing more efficient and stable bio-scaffolds.

1. Introduction

The extracellular matrix (ECM) is an intricate network of macromolecules synthesized and secreted by different cells. Serving as the microenvironment for cellular existence, it not only provides structural support but also influences cellular functions by modulating signal transduction pathways [1–3]. Dysregulation of ECM can lead to multiple diseases and is even implicated in the metastasis of tumors [4–8]. A significant application of ECM is being made into biological scaffolds by various decellularization methods, promising in tissue regeneration and reconstruction [2].

Bio-scaffolds derived from natural proteins, such as collagen, fibrin, elastin, and silk fibroin [9–11], demonstrate superior biocompatibility compared to synthetic scaffolds. However, they cannot regenerate tissue in vivo and typically require the seeding of stem cells. In contrast, ECM-based scaffolds produced using decellularization technology retain the ultrastructure and bioactive components of the native tissue, enabling spontaneous tissue regeneration upon implantation in the body [2]. Decellularization techniques have been employed to fabricate extracellular matrix (ECM) bioscaffolds from a variety of tissues, including adipose tissue [2], dermis [12], trachea [13], small intestinal mucosa [14], cartilage [15,16], lung [17–19], kidney [20,21], and pericardium [22,23]. Among these, the decellular adipose-derived matrix (DAM) is most readily accessible in clinical practice and is considered the most promising scaffold material for soft tissue regeneration [24]. At Present, the effect of adipogenesis of DAM varied widely after

* Corresponding author.
** Corresponding author.
E-mail addresses: liuchunjun@psh.pumc.edu.cn (C. Liu), luanjie@psh.pumc.edu.cn (J. Luan).
[1] Xiaomu **Ma** and Qiang **Yue** have contributed equally to this work and share the first authorship.
[2] Chunjun **Liu** and Jie **Luan** have contributed equally to this work and share the role of corresponding authors.

https://doi.org/10.1016/j.mtbio.2024.101235
Received 6 August 2024; Received in revised form 2 September 2024; Accepted 7 September 2024
Available online 12 September 2024

transplantation in vivo among different studies, making it difficult to make a horizontal comparison [25–28]. This suggests that even ECM from the same tissue can exhibit various properties influenced by the donor site. As an important endocrine organ, adipose tissue participates in many physiological functions, including energy metabolism and hormone secretion [29]. Thus, DAM not only comprises macromolecules such as collagen and proteoglycans but also hosts a diverse array of adipokines which play an important role in adipogenesis [29]. Adipose tissue from different donor sites possesses distinct functions, and the ECM can vary accordingly. Studies have shown that DAM derived from porcine subcutaneous and visceral adipose tissues contains different types of collagen and exhibits varying degrees of stiffness, which contributes to their differing adipogenic effects [30]. However, there is a lack of research elucidating distinctions between human DAM from different regions of adipose tissue, which limits our understanding of the structural and functional heterogeneity of adipose tissue and poses challenges for the clinical translation of DAM.

Human-derived DAM is most commonly available from subcutaneous fat, especially abdominal region, with a wide range of sources including liposuction and abdominoplasty. Subcutaneous adipose tissue (SAT) is further divided into superficial SAT (sSAT) and deep SAT (dSAT) by the Scarpa's fascia. Numerous studies have reported distinct roles of adipocytes and stem cells from sSAT and dSAT in metabolic disorders and tissue engineering applications [31,32]. However, no study has investigated the differences between ECMs derived from sSAT and dSAT. Structurally, sSAT is characterized by closely packed, regular cubic lobules, whereas dSAT features flattened, irregular lobules [33]. Functionally, dSAT is intimately linked to insulin resistance, type 2 diabetes, and cardiovascular diseases, resembling visceral adipose tissue in its mechanisms, whereas sSAT shows no overt association [32,34,35]. Adipose-derived stem cells (ADSCs) from sSAT exhibit faster proliferation rates and possess stronger multilineage differentiation potential, indicative of more robust stem cell characteristics [36,37], thereby making them more suitable for applications in stem cell-based tissue engineering [38]. Our previous findings reveal variations in the in situ oxygen concentration and survival rates of fat grafts between sSAT and dSAT. Given the substantial evidence of disparities between deep and superficial fat depots, we speculate that their ECMs also exhibit differential characteristics, potentially associated with their distinct endocrine functionalities.

To validate this hypothesis, we made superficial DAM (S-DAM) and deep DAM (D-DAM) using abdominal deep and superficial fat tissues from healthy females within certain ages, BMI, and abdominal fat thickness. For the first time, we demonstrated differences in the physical-mechanical properties, composition, and adipogenic induction potential of ECMs derived from these distinct adipose layers. Moreover, our findings suggest a potential direct correlation between metabolic status and regenerative properties. We believe that these discoveries not only open new avenues for the design of regenerative therapies but also provide new perspectives for profound interconnections between metabolic health and regenerative medicine.

2. Method

2.1. Abdominal fat harvesting

Abdominal adipose tissue was collected from healthy females who received abdominoplasty. Patients were 25–45 years old with BMI from 20 kg/m^2 to 24 kg/m^2. The adipose tissue on both sides of Scarpa fascia was separated with scissors and recorded as group S (Superficial) and group D (Deep), respectively. The adipose tissue was then soaked in PBS and cut as finely as possible, then rinsed with water and centrifugation. The fat layer was collected and used to make ECM. The use of adipose tissue was approved by the Ethics Committee of the Plastic Surgery Hospital of the Chinese Academy of Medical Sciences (No. ZX201843).

2.2. Preparation of S-DAM and D-DAM

The collected adipose tissue was homogenized for 2–3 min until there were no visible particles. Centrifuge the suspension at 3500 g for 3 min and discard the oil layer. The remaining part was pre-DAM and received decellularization by Enzyme-free method as previously reported method. In brief, pre-DAM was soaked in 0.5 M NaCl, 1 M NaCl, sterile distilled water, and 1 % Triton-X100 solution in a constant temperature shaker (37 °C, 100 rpm) for 4 h, 4 h, 10 h, and 48 h in sequence. Then rinse with sterile distilled water three times with 0.5 h each, and shake in 99 % isopropanol for 6 h. Finally, DAM was washed with sterile distilled water and sterilized with 75 % alcohol 3 times. DAM was lyophilized at −80 °C for 72 h and stored at 4 °C.

2.3. DNA quantification

The lyophilized DAM was weighed and extracted using extract buffer DNeasy Kit™ (Qiagen). A working solution was added and incubated for 5–10 min at 37 °C. The residual DNA (ng/mg dry weight) of DAM was quantified with a microplate reader (Model 680; Bio-Rad) at 260 nm. The samples were normalized to the initial dry weight (n = 5).

2.4. Histology

Hematoxylin and eosin (H&E) staining and Masson's trichrome were performed according to standard protocols. Immunohistochemistry staining for HSP60 (ab190828), immunofluorescence staining for perilipin (ab3526; Abcam), CD31 (ab182981; Abcam), Collagen I (ab34710; Abcam), Collagen XIV (abs130429; Absin), and laminin beta 1 (ab108536; Abcam) was performed using appropriate secondary antibodies.

2.5. Scanning electron microscopy (SEM)

For SEM, the lyophilized DAM or co-cultured complex was fixed with 2.5 % glutaraldehyde and received gradient dehydration (20%- 50%-70%-90%-100 %, 10min each, 100 % twice). The samples were then lyophilized and sputtered with gold for 300s. Image-Pro Plus 6.0 software (Media Cybernetics, Inc., Rockville, MD, USA) was used to measure the pore diameter (μm) with a 100 μm (x 300) scale as the standard.

2.6. Secant modulus

Stiffness was tested using a 5967 universal testing machine with a 100 N load sensor (Instron, Norwood, MA). The lyophilized DAM was cut into discs with 5 mm diameter using a corneal trephine, and compressed by the indenter at a speed of 10 mm/min (n = 3). The stress-strain curves were recorded and analyzed to determine the secant modulus at strain values of 0.3–0.9 mm/mm respectively.

2.7. Enzyme-linked immunosorbent assay (ELISA)

To measure the total protein concentration, DAM was extracted with a BCA protein assay kit (P0012; Beyotime). Growth factor and chemokines including basic fibroblast growth factor (bFGF) (LV10055), Platelet-Derived Growth Factor BB Homodimer (PDGF-BB) (LV10404), VEGF (LV10533), C-X-C Motif Chemokine Ligand 12(CXCL12) (LV11330) and C-C Motif Chemokine Ligand 21(CCL21) (LV10083) were quantified by ELISA (Animal Union, R&D) (n = 3).

2.8. Animal studies

Fifteen female Balb/c nude mice (6–8 weeks old, 10125) were purchased from Beijing Vital River Laboratory Animal Technology Company. Each mouse received two injections (left: S-DAM, right: D-DAM). For each injection, 5 mg (dry weight) DAM was soaked in 200 μl normal

saline and thoroughly cut, followed by injected subcutaneously on the dorsal regions using 18-gauge needles. Mice were euthanized after 4 weeks, 8 weeks, and 12 weeks ($n = 5$ per group). All animal experiments were carried out in accordance with the National Institutes of Health guide for the care and use of Laboratory animals (NIH Publications No. 8023, revised 1978), and were approved by The Chinese Academy of Medical Sciences and Peking Union Medical College animal ethics committee [2023(2)].

2.9. In vitro studies

2.9.1. Co-culture of ADSCs and DAM

Human adipose-derived stem cells (ADSCs) were prepared from lipoaspirate. ADSCs were isolated by 0.1 % type I collagenase at 37 °C for 45 min and cultured in Dulbecco's modified Eagle's medium (DMEM) containing 10 % fetal bovine serum (FBS). Passage 3 of ADSCs was used. For three-dimensional co-culture, sterile lyophilized DAM (5 mg) was seeded with 30 μl of cell suspension (1×10^5 ADSCs). When the suspension was fully absorbed by DAM, the complex was transferred to a new 24-well plate and cultured with DMEM.

2.9.2. Evaluation of cell adherence and cell activity

After cultured with DMEM for 24 h, cell adherence was evaluated with SEM. CCK8 was used to quantify the cell adherence rate and cell activity. When performing CCK8 testing, a 400 μl working solution (CCK8: DMEM = 1:10) was added and incubated with the complex at 37 °C for 2 h. The OD value at a wavelength of 450 nm was measured by ELISA (Thermo Fisher Scientific, USA). The OD value before and after the transferring of the complex was recorded as OD1 and OD2, respectively. The cell adherence rate was calculated as OD2/OD1*100 % (n = 5). After transferring, the complex was cultured with Mesenchymal Stem Cell Medium (MSCM, 7501, ScienCell) for 9 days. CCK8 testing was performed at the same time point every 2 days (n = 5).

2.9.3. Immunofluorescence staining of Bodipy

After seeding ADSCs and cultured with MSCM for 6 days, the complex was induced by a human adipogenic mesenchymal stem cells lipogenesis induction differentiation kit (HUXMD-90031, Oricell, CN) for 14 days. A working solution of Hoechst 33342+Bodipy (Thermo, United States) was prepared according to the kit protocol. Shake the complex with the working solution in the dark for 30 min (n = 3). Capture images for observation with a Confocal fluorescence microscope (Leica, Allendale, N.J).

2.10. Proteomic

The total protein in DAM was extracted and divided for total protein concentration measurement and trypsin enzymolysis. After desalting the enzymolysis peptide segment, the samples were identified by LC-MS/MS (4D-DIA). Data was imported to Spectronaut Pulsar 18.4 (Biognosys) for analysis. Proteins with a fold change ratio ≥1.5 or ≤1/1.5 and *P*-value <0.05 were defined as differentially expressed proteins. Gene Ontology (GO) and Kyoto Encyclopedia of Genes and Genomes (KEGG) analysis are used to perform functional enrichment of differentially expressed genes. Gene Set Enrichment Analysis (GSEA) was performed on the full set of genes, inclusive of those without differential expression, to investigate comprehensive enrichment profiles. Protein-protein interaction (PPI) network was constructed using the STRING database, from which non-functional proteins were removed.

2.11. Statistical analysis

All data were analyzed using SPSS Statistics software 27 (IBM, USA) and expressed as the mean ± standard deviation (SD). Student's t-test and one-way ANOVA were used after the test of normality. Statistically significant differences were indicated as follows: *, $p < 0.05$; **, $p < 0.01$; and ***, $p < 0.001$.

3. Results

3.1. Acquisition, appearance, and decellularization of S-DAM and D-DAM

Superficial and deep adipose tissues were separately dissected from the Scarpa's fascia (Fig. 1A) and were then cut into small pieces approximately 0.5 mm in diameter in PBS. After rinsing with PBS and centrifugation, it was observed that the wash solution of the deep group was redder (Fig. 1B), indicating a higher concentration of red blood cells. Continued rinsing with PBS until the wash solution became clear and transparent (Fig. 1C), followed by homogenization and centrifugation. It was found that the ECM from superficial adipose tissue showed a white color while the ECM from the deep layer appeared brown (Fig. 1D). Post-decellularization, the S-DAM was visibly whiter with a finer texture, whereas the D-DAM retained relatively darker with a coarser texture (Fig. 1E–F).

3.2. Different structures of S-DAM and D-DAM

H&E (Fig. 2A) and SEM (Fig. 2B) revealed that the pores in S-DAM are significantly larger, averaging 70.0 ± 18.4 μm (Fig. 2C). The pore arrangement is relatively loose and cubic in shape (Fig. 2A–B). In contrast, the pore diameter in D-DAM was 55.6 × 19.9 μm, with a tighter arrangement and an oblate shape. Under high magnification of SEM, both S-DAM and D-DAM exhibit rough surfaces, but D-DAM shows a greater degree of roughness, with ECM twisted and entangled, creating an extremely uneven surface (Fig. 2B). Masson's trichrome staining indicated a higher content of muscle fibers in D-DAM (Fig. 2A).

3.3. D-DAM exhibits higher stiffness

It was found that S-DAM and D-DAM exhibited nonlinear material properties. Specifically, focusing on the strain range from 0.2 to 0.8 mm, the secant modulus of S-DAM was consistently lower than that of D-DAM (Fig. 2D). This indicates that within this particular strain interval, S-DAM demonstrates less stiffness compared to D-DAM.

3.4. Constituents analysis

3.4.1. Cytokines

The DNA content in the S-DAM and D-DAM was 31.18 ± 3.32 ng/mg and 40.77 ± 5.90 ng/mg($p > 0.05$) (Fig. 3A), respectively, both conforming to the standards for decellularized matrix materials. The growth factors including bFGF ($p = 0.000$) and VEGF ($p = 0.026$) were significantly higher in S-DAM compared to D-DAM (Fig. 3B). There was no significant difference in PDGF-BB between the two groups ($P > 0.05$) (Fig. 3B). Similarly, the chemokines CXCL12 ($p = 0.027$) and CCL12 ($p = 0.008$) were significantly more abundant in S-DAM than in D-DAM (Fig. 3C).

3.4.2. Proteomics

3.4.2.1. Cellular and extracellular different proteins and functional enrichment. The proteomic profiles of S-DAM and D-DAM exhibit substantial differences, with 1115 proteins demonstrating significant differential expression (Fig. 3D). Specifically, 696 proteins were notably decreased in S-DAM relative to D-DAM, whereas 419 proteins were significantly increased (Fig. 3D). The ECM comprises not only secreted proteins including collagens and proteoglycans but also components of the basement membrane, along with the interstitial, connective tissue matrix and the cellular debris that it envelops. Enzymatic-free decellularization protocol we used could largely preserve these components,

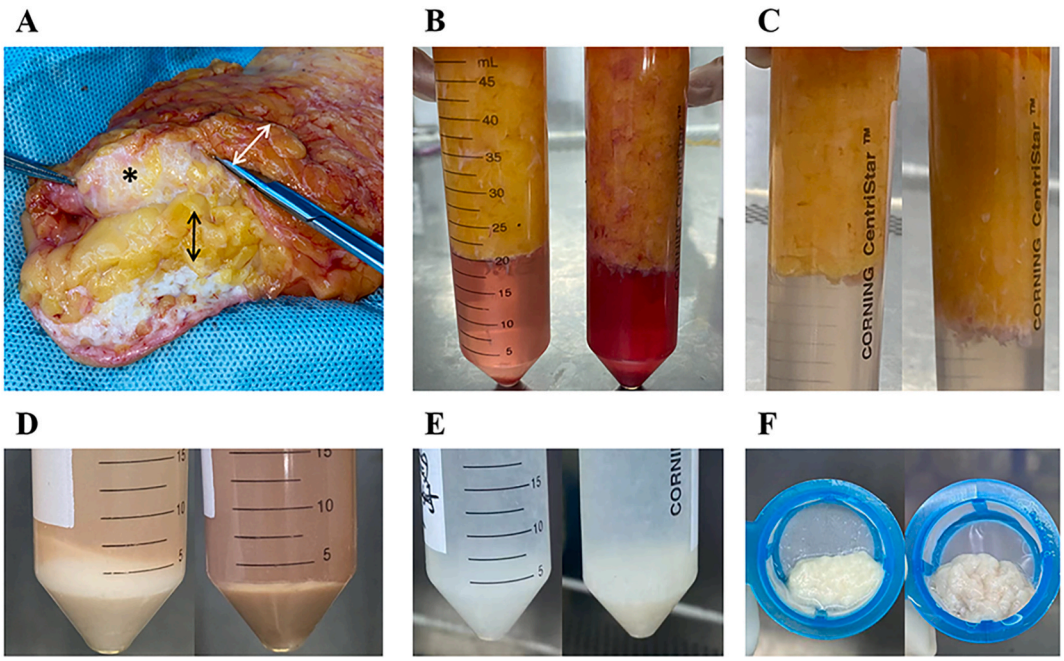

Fig. 1. Preparation and appearance of S-DAM and D-DAM. A. Specimen of abdominal subcutaneous adipose tissue. Asterisk: Scarpa's fascia. Black arrow: the superficial layer of abdominal adipose tissue. White arrow: the deep layer of abdominal adipose tissue. B. The First rinse and centrifugation of superficial (left) and deep (right) layers of adipose tissue after being cut into small pieces with 0.5 mm diameter. C. The third rinse of superficial (left) and deep (right) layers of adipose tissue. D. Pre-S-DAM (left) and pre-D-DAM (right) after physical crushing and centrifugation. E-F. Appearance of S-DAM (left) and D-DAM (right) before lyophilization.

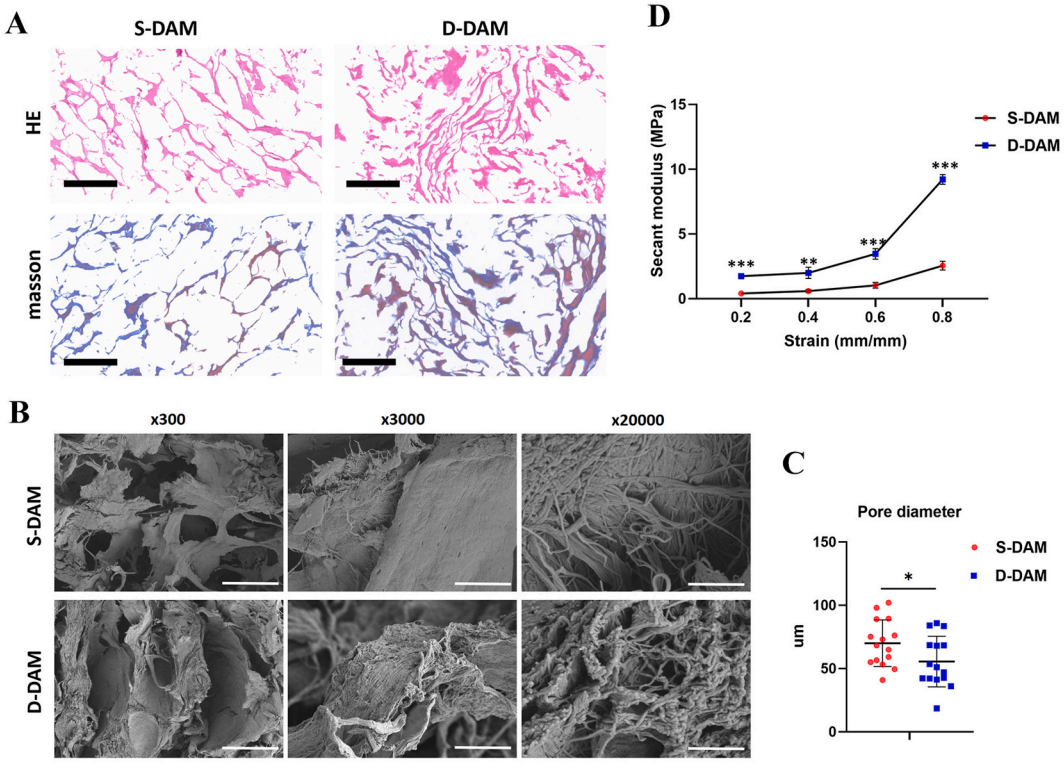

Fig. 2. Microstructure and mechanical properties of S-DAM and D-DAM. A. HE and Masson staining of S-DAM and D-DAM. Scale bar = 500μm. B. Scanning electron microscopy image of lyophilized S-DAM and D-DAM. Scale bar = 100μm, 10 μm and 2 μm, respectively. C. Quantitative analysis of pore diameter in S-DAM and D-DAM. (n = 15) D. Secant modulus of S-DAM and D-DAM. (n = 3) Data are expressed as the mean ± standard error, and p-values are calculated using Student's t-test. ns: not significant. *: $p < 0.05$, **: $p < 0.01$, ***: $p < 0.001$.

which were detected in proteomics data (Figure E–F) and enabled a comprehensive analysis of the composition of ECM.

The main components of the ECM, collagen-associated proteins, were analyzed first using GO analysis. Both increased and decreased terms were found (Fig. 3E), indicating distinct collagen profiles between S-DAM and D-DAM. S-DAM predominantly featured collagens I and II

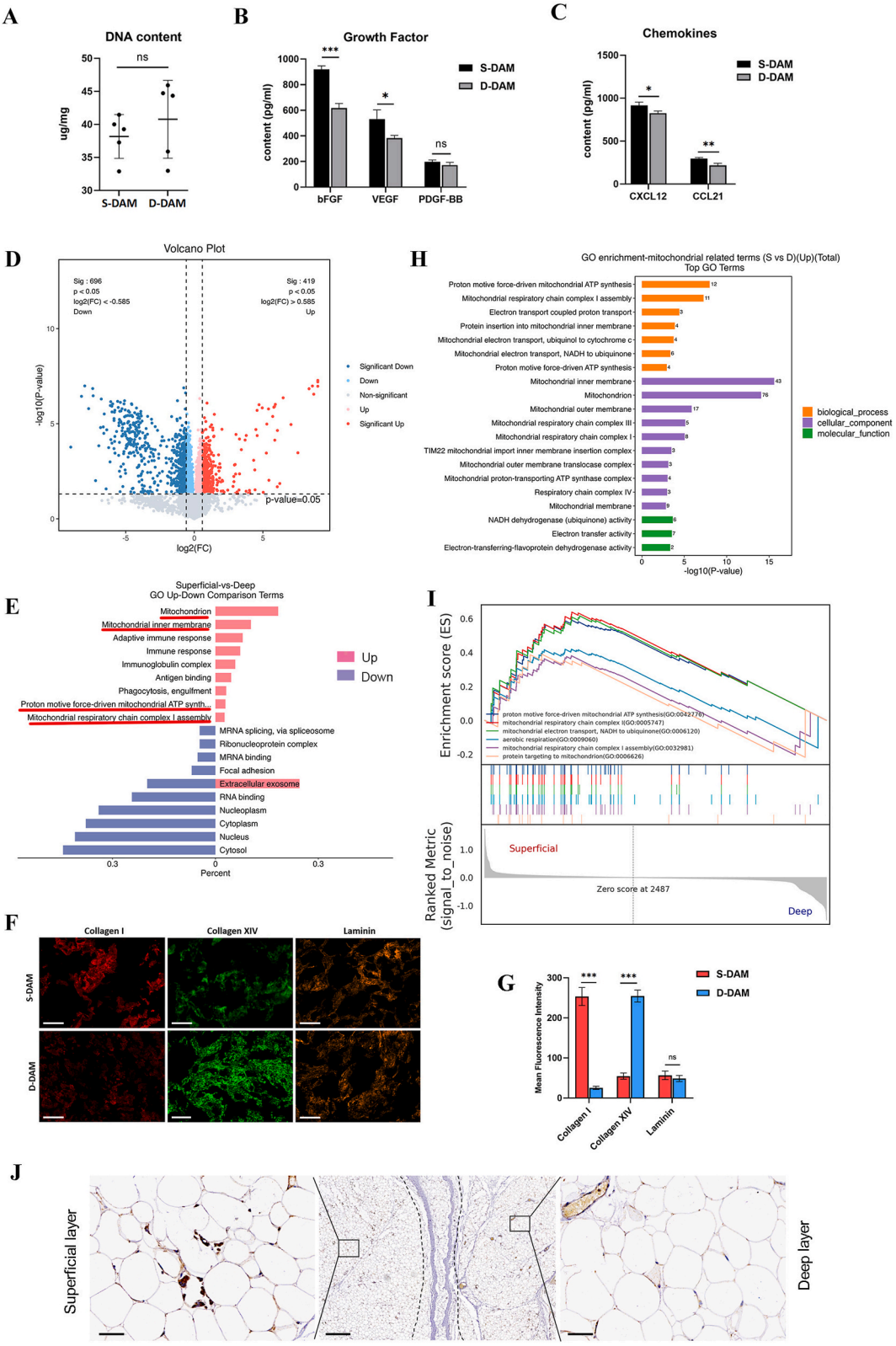

Fig. 3. Composition analysis of S-DAM and D-DAM. A. DNA content of S-DAM and D-DAM. (n = 5) B. ELISA analysis of bFGF, VEGF, and PDGF-BB. (n = 3) C. ELISA analysis of CXCL12 and CCL21. (n = 3) D. Volcano Plot showed a global protein profile of S-DAM and D-DAM. E. Top 10 most different terms in GO enrichment. F-G. Immunofluorescence of Collagen I, Collagen XIV, and Laminin in the L-DAM and D-DAM groups. (n = 3) H. GO enrichment of mitochondrial-related terms significantly increased in the S-DAM group. I. GSEA analysis of terms associated with mitochondrion. J.HSP-60 immunohistochemistry staining of Superficial and deep layer of abdominal adipose tissue. Dash line region: Scarpa's fascia. Scale bar = 50 μm, 500 μm, 50 μm. Data are expressed as the mean ± standard error, and p-values are calculated using Student's t-test. ns: not significant. *: $p < 0.05$, **: $p < 0.01$, ***: $p < 0.001$.

Table 1
Extracellular matrix-associated proteins that significantly increased in S-DAM compared with D-DAM.

ID	Terms	P value	Swiss-Prot	Gene	Protein
GO:0005585	collagen type II trimer	0.0215	P02458	COL2A1	Collagen alpha-1(II) chain
GO:0005584	collagen type I trimer	0.0425	P02452	COL1A1	Collagen alpha-1(I) chain
GO:0062023	collagen-containing extracellular matrix	0.0428	P01011	SERPINA3	Alpha-1-antichymotrypsin
			P02675	FGB	Fibrinogen beta chain
			P07711	CTSL	Procathepsin L
			P09382	LGALS1	Galectin-1
			P19652	ORM2	Alpha-1-acid glycoprotein 2
			Q92954	PRG4	Proteoglycan 4
			Q9H239	MMP28	Matrix metalloproteinase-28
			P15088	CPA3	Mast cell carboxypeptidase A
			P02647	APOA1	Apolipoprotein A-I
			P02671	FGA	Fibrinogen alpha chain
			P02679	FGG	Fibrinogen gamma chain

(Table 1), whereas D-DAM was characterized by an abundance of collagen XIV (Table 2). No significant differences were observed for proteins related to collagen IV, XI, and laminin (Table 3). Immunofluorescence confirmed the content of Collagen I, Collagen XIV, and Laminin in both groups (Fig. 3F–G). GSEA of the collagen-containing extracellular matrix (GO:0062023) did not reveal any significant differences between S-DAM and D-DAM.

Next, significantly increased terms in the S-DAM group were analyzed. Proteins associated with mitochondria and immune-inflammatory responses exhibited the most pronounced differences (Fig. 3E). Significantly increased mitochondria-associated terms were shown from Biological Process (BP), Cellular Component (CC), and Molecular Function (MF) (Fig. 3H). Among 20 terms, the mitochondrial inner membrane (GO:005743) showed the largest significance (Fig. 3G). GSEA was then used to analyze mitochondria-related terms, and six terms with Normalized Enrichment Scores (NES) $\geq$1.5 were found (Fig. 3I). More mitochondria in the superficial layer than in the deep layer were confirmed by immunohistochemistry (Fig. 3J). Among terms markedly reduced in the S-DAM group, we observed that those with the largest differential significance were predominantly linked to RNA processing (Fig. 3E).

Table 3
Extracellular matrix-associated terms that have no significant difference between S-DAM and D-DAM.

ID	terms	Swiss-Prot	Gene	Protein
GO:0005592	collagen type XI trimer	P02458	COL2A1	Collagen alpha-1(II) chain
GO:0005587	collagen type IV trimer	P02462	COL4A1	Collagen alpha-1 (IV) chain
GO:0043236	laminin binding	P09382	LGALS1	Galectin-1
GO:0038064	collagen receptor activity	P17301	ITGA2	Integrin alpha-2
GO:0030199	collagen fibril organization	P49747	COMP	Cartilage oligomeric matrix protein
GO:0032963	collagen metabolic process	Q63HR2	TNS2	Tensin-2

3.4.2.2. More neuron and vessel components were found in S-DAM. Among terms markedly reduced in the S-DAM group, numerous terms associated with neural, muscle, and vessel were identified, with the top 10 significantly reduced terms shown as bubble plots (Fig. 4A and B).

Table 2
Extracellular matrix-associated proteins significantly decreased in S-DAM compared with D-DAM.

ID	Terms	P value	Swiss-Prot	Gene	Protein
GO:0005518	collagen binding	0.0016	O43405	COCH	Cochlin
			P49747	COMP	Cartilage oligomeric matrix protein
			Q9BXN1	ASPN	Asporin
			Q9H6X2	ANTXR1	Anthrax toxin receptor 1
			Q9UKZ9	PCOLCE2	Procollagen C-endopeptidase enhancer 2
GO:0005596	collagen type XIV trimer	0.0358	Q05707	COL14A1	Collagen alpha-1(XIV) chain
GO:0032964	collagen biosynthetic process	0.0477	P50454	SERPINH1	Serpin H1
GO:0062023	collagen-containing extracellular matrix	0.0010	O43405	COCH	Cochlin
			P00488	F13A1	Coagulation factor XIII A chain
			P00748	F12	Coagulation factor XII
			P02462	COL4A1	Collagen alpha-1(IV) chain
			P05452	CLEC3B	Tetranectin
			P08294	SOD3	Extracellular superoxide dismutase [Cu-Zn]
			P08493	MGP	Matrix Gla protein
			P15502	ELN	Elastin
			P21810	BGN	Biglycan
			P36955	SERPINF1	Pigment epithelium-derived factor
			P52272	HNRNPM	Heterogeneous nuclear ribonucleoprotein M
			P60903	S100A10	Protein S100-A10
			Q05707	COL14A1	Collagen alpha-1(XIV) chain
			Q13361	MFAP5	Microfibrillar-associated protein 5
			Q7Z7G0	ABI3BP	Target of Nesh-SH3
			Q8N474	SFRP1	Secreted frizzled-related protein 1
			P35556	FBN2	Fibrillin-2
			Q96HD1	CRELD1	Protein disulfide isomerase CRELD1
			Q99969	RARRES2	Retinoic acid receptor responder protein 2
			Q99972	MYOC	Myocilin
			Q9UBX5	FBLN5	Fibulin-5
			Q9UKU9	ANGPTL2	Angiopoietin-related protein 2

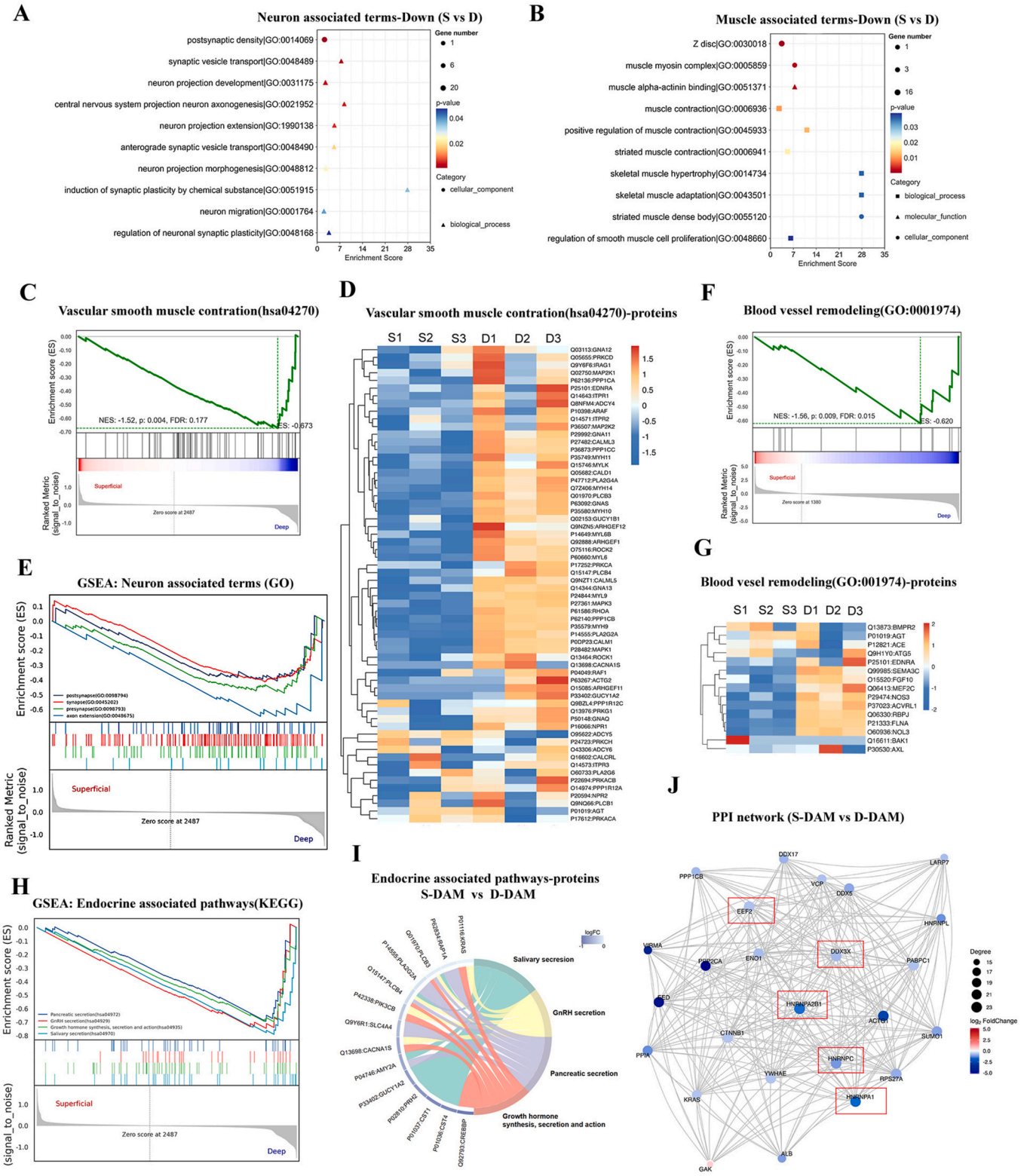

Fig. 4. Proteomic analysis of S-DAM and D-DAM. A. Neuron-associated terms significantly decreased in the S-DAM group. B. Muscle-associated terms significantly decreased in the S-DAM group. C. GSEA analysis of vascular smooth muscle contraction pathway. D. All proteins and their abundance in the pathway of vascular smooth muscle contraction. E. GSEA of neuron-associated terms which were significantly decreased in the S-DAM group. F. GSEA analysis of blood vessel remodeling term. G. All proteins and their abundance in blood vessel remodeling term. H. GSEA of endocrine-associated pathways which were significantly decreased in the S-DAM group. I. Proteins in each endocrine-associated pathway which was significantly decreased in the S-DAM group. J. PPI network of S-DAM and D-DAM. Red box: genes involved in mRNA processing.

GSEA analysis was used to analyze the corresponding terms. Notably, in the muscular category, the vascular smooth muscle contraction (hsa04270) term was significantly decreased in the S-DAM group (Fig. 4C–D). Regarding neural components, four terms including synapse (GO:0045202), presynapse (GO: 0098793), postsynapse (GO: 0098794), and axon extension (GO: 0048675) were identified as significantly decreased in the S-DAM group (Fig. 4E). In the vascular category, the blood vessel remodeling (GO: 0001974) term was notably decreased (Fig. 4F–G).

3.4.2.3. More endocrine-associated proteins were found in D-DAM. Furthermore, through GSEA-KEGG analysis, we unveiled that the D-DAM demonstrated a significantly greater involvement in endocrine-associated pathways, including Salivary secretion (hsa04970), Pancreatic secretion (hsa04972), GnRH secretion (hsa04929), and Growth hormone synthesis, secretion and action (hsa04935) (Fig. 4H). The corresponding proteins were listed in the chord diagram (Fig. 4I). Additional pathways, including Insulin secretion (hsa04911), Renin secretion (hsa04924), Parathyroid hormone synthesis, secretion and action (hsa04928), Aldosterone synthesis and secretion (hsa04925), and Gastric acid secretion (hsa04971), also displayed NES greater than 1. However, the False Discovery Rate (FDR) values for these pathways were over 0.25.

3.4.2.4. PPI network analysis. PPI network analysis was employed to elucidate interactions among proteins with the highest differential significance (Fig. 4J). Ninety percent of these proteins were significantly more abundant in D-DAM compared to S-DAM, Fifty percent of which

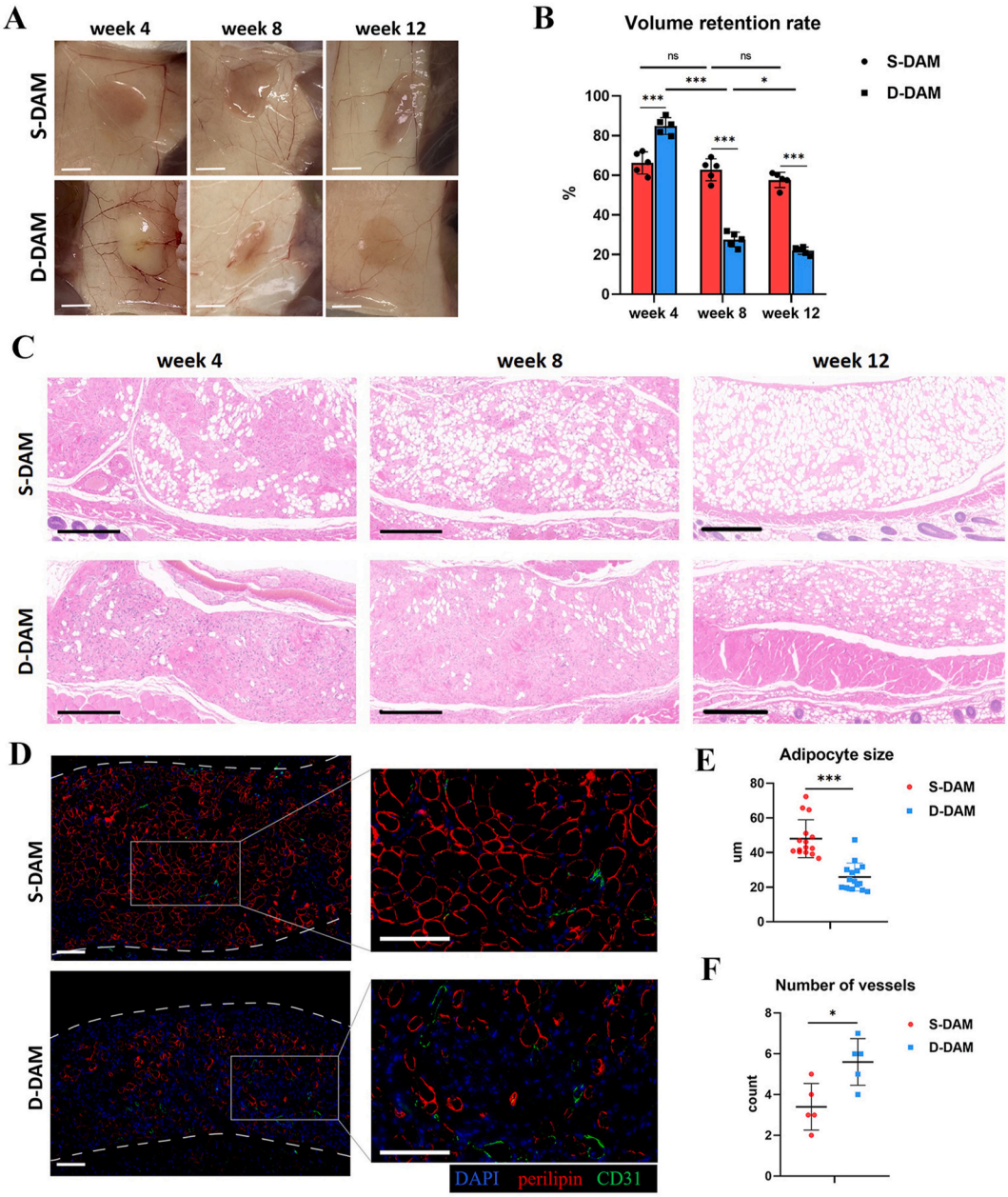

Fig. 5. S-DAM had a better ability for adipogenesis than D-DAM. A. Macroscopic image of S-DAM and D-DAM at 4 weeks, 8 weeks, and 12 weeks after implantation. B. Volume retention rate of S-DAM and D-DAM. (n = 5) C. HE staining of the scaffold. Scale bar = 500 μm. D. Immunofluorescence co-localization of perilipin and CD31 of the scaffold at 12 weeks after implantation. Scale bar = 100μm. E. The size of adipocyte on the perilipin staining 12 weeks after implantation. (n = 15) F. Number of vessels on the CD31 staining 12 weeks after implantation. (n = 5) Data are expressed as the mean ± standard error, and p-values are calculated using Student's t-test. ns: not significant. *: $p < 0.05$, ***: $p < 0.001$.

were implicated in mRNA processing, mRNA stability, and nuclear export. Among them, Heterogeneous nuclear ribonucleoproteins A2/B1 (HNRNPA2B1), Heterogeneous nuclear ribonucleoprotein A1 (HNRNPA1), and Heterogeneous nuclear ribonucleoproteins C1/C2 (HNRNPC) primarily function by binding to pre-mRNAs, packaging them into heterogeneous nuclear ribonucleoprotein (hnRNP) particles, and facilitating their transport from the nucleus to the cytoplasm [39–46]. Additionally, Elongation factor 2 (EEF2) and the ATP-dependent RNA helicase (DDX3X) play roles in RNA unwinding and catalyze ribosomal translocation during the process of translation elongation [47,48].

3.5. S-DAM demonstrated superior adipogenesis but inferior angiogenesis in vivo

Post-implantation, both S-DAM and D-DAM exhibited good tissue compatibility. At 4 weeks post-implantation, S-DAM was soft and pink visibly, whereas D-DAM was harder and yellowish-white in color (Fig. 5A). By 8 weeks, the volume retention rate of S-DAM showed no significant decrease (Fig. 5B), with its color and texture resembling normal adipose tissue (Fig. 5A). Conversely, the volume retention rate of D-DAM began to markedly decline after 4 weeks (Fig. 5B), with the tissue becoming transparent and flattened by 12 weeks (Fig. 5A). H&E staining indicated that the adipogenic area of S-DAM was consistently larger than that of D-DAM across all time points (Fig. 5C). IF staining of perilipin at 12 weeks post-implantation revealed that both adipogenic area and adipocyte size were significantly larger in the S-DAM group than in the D-DAM group (Fig. 5E). Surprisingly, number of vessels in the S-DAM group was less than that of D-DAM (Fig. 5F). This suggests that angiogenesis does not necessarily promote adipogenesis, and the superior adipogenic effect of S-DAM was unrelated to its angiogenic capacity.

3.6. In vitro experiments

3.6.1. Cell adhesion rate and viability

After seeding ADSCs on DAM scaffolds for 24 h, the adhesion rate for S-DAM was 79.4 %, while it was 72.8 % for D-DAM. There was no significant difference between the two ($p = 0.11$) (Fig. 6A). SEM revealed that cells established microfilament connections with both DAM scaffolds; however, cells on D-DAM appeared flatter compared to those on S-DAM, which maintained a more stereo structure (Fig. 6B). ADSCs seeded on S-DAM demonstrated higher cell proliferation activity compared with D-DAM (Fig. 6C).

3.6.2. Enhanced adipogenic capacity of S-DAM in vitro under inductive conditions

After 14 days of adipogenic induction, S-DAM groups were able to generate large, round unilocular lipid droplets. In contrast, D-DAM produced scattered and smaller lipid droplets (Fig. 6D). These findings confirmed that S-DAM has a stronger potential for adipogenic differentiation compared to D-DAM. The enhanced ability of S-DAM to support adipogenic differentiation may be attributed to its specific structural properties or preserved bioactive cytokines that better facilitate ADSC adhesion, spreading, and subsequent differentiation into mature adipocytes.

4. Discussion

ECM plays a pivotal role in maintaining tissue architecture, regulating cellular behavior, and participating in numerous physiological and pathophysiological processes [49]. Abnormalities in ECM are implicated in a myriad of diseases, including cardiovascular diseases, fibrotic disorders [4–6], and sarcopenia [50]. Furthermore, ECM can direct the differentiation trajectory of stem cells, which is vital for wound healing and tissue regeneration [2,51–55]. In addition, ECM-based biomaterials are extensively employed in tissue engineering for fabricating artificial tissues and organs. Therefore, research on ECM is of paramount importance [56].

Abdominal sSAT and dSAT have been reported to play distinct roles in metabolic disorders and energy homeostasis [31,32,34,35,57], yet if there is a difference in ECM between these fat compartments has remained unexplored. Our study revealed marked differences in the physical-mechanical properties and compositional profiles of ECMs derived from sSAT and dSAT for the first time. Notably, DAM obtained from sSAT demonstrates a superior property to induce adipose tissue regeneration. We believe these findings not only deepen our comprehension of the structural and functional heterogeneity of adipose tissues but also introduce innovative perspectives and potential applications within the realm of adipose tissue regenerative medicine.

Physical mechanical properties are crucial factors in the extracellular microenvironment [51,58]. We found that S-DAM exhibits looser pores with cubic shapes and lower material hardness, which is conducive to the cushioning and insulation functions provided by sSAT. Conversely, D-DAM displays denser pores with flatter shapes, increased material stiffness, and a higher content of cytoskeletal components. These characteristics of deep ECM facilitate support and stabilization of internal structures, thereby withstanding mechanical stresses and internal pressures, such as preventing herniation formation. In tissue engineering, mechanical signals from the ECM can be transduced into biochemical

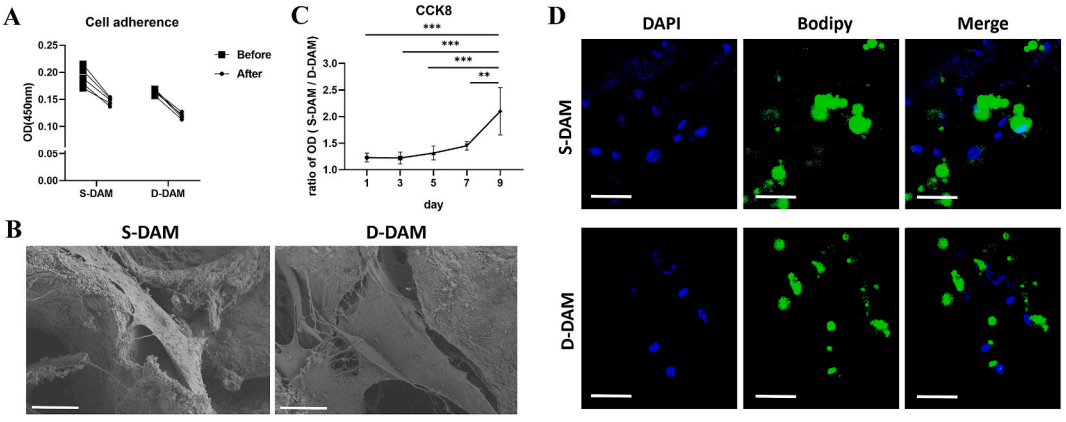

Fig. 6. Co-culture of ADSCs and DAM in vitro. A. CCK-8 testing of the S-DAM and D-DAM group before and after being transferred to a new 24-well plate 24 h after seeding. (n = 5) B. Scanning electron microscopy image of the complex after 24 h of co-culture. Scale bar = 10μm. C. CCK-8 testing of the S-DAM and the D-DAM group during 9 days'co-culture. (n = 5) D. Immunofluorescence staining of Bodipy after 14 days of lipogenesis induction. Scale bar = 50μm. Data are expressed as the mean ± standard error, and p-values are calculated using one-way ANOVA. **: $p < 0.01$, ***: $p < 0.001$.

signals, influencing cell differentiation through impacts on cell adhesion and cytoskeletal function [59–61]. Some studies have engineered microenvironments with specific mechanical cues to design biomaterials with inducible properties [62,63]. Chandler et al. fabricated photo-crosslinked alginate hydrogels and demonstrated that as the stiffness of the biomaterial increased, the adipogenic differentiation potential of ADSCs decreased, while angiogenesis capacity was enhanced [64]. Young et al. reached similar conclusions, proposing that scaffolds with mechanical strength closest to native adipose tissue exhibit the greatest potential for inducing adipose tissue regeneration [65]. This aligns with our observation that the harder D-DAM exhibits inferior regenerative capability. Even more, S-DAM possesses larger pores, with a higher prevalence of pores in the range of 60–200 μm, which facilitates better cell adhesion [66]. Moreover, both S-DAM and D-DAM present rough surfaces, with D-DAM exhibiting a greater degree. A rough surface of the material can provide ample physical anchoring points for cells, favoring cell adhesion. However, an excessively rough surface may damage the cell membrane or impair normal cellular functions, which could be one reason underlying the reduced adipogenic potential of D-DAM.

Compositionally, S-DAM and D-DAM exhibit substantial discrepancies. Firstly, while the total content of the predominant component, collagen-related proteins, is comparable, the primary collagen types differ. Secondly, our findings reveal a higher abundance of proteins associated with neural and vascular elements in the stroma of dSAT. Conversely, previous studies show that sSAT is intimately linked to the nutritional and sensory functions of the skin, featuring a richer vasculature and innervation to supply nutrients, oxygen, and convey tactile and thermal sensory information [67]. The discrepancy in these conclusions may stem from the fact that superficial nerves, related to cutaneous sensation, are largely embedded within retinacula-cutis (RC), a loose collagenous network immediately beneath the dermis [68]. These structures, being more intimately associated with the dermis, are less likely to be included in surgically harvested fat tissue and thus were not part of our study. The distribution of nerve fibers within adipose tissue not only regulates energy metabolism and controls lipid deposition and lipolysis but also contributes to local blood flow regulation and sensory transmission [67]. The lower neural density in superficial fat may imply lesser sensitivity in perception and response compared to deep fat, consistent with its primarily static functions such as insulation and mechanical buffering [67]. Deep adipose tissue, closely associated with locomotion and thermoregulation [67], showed a rich neurovascular network that may facilitate rapid responses to external stimuli and dynamic energy regulation. Conversely, superficial adipose tissue might rely more heavily on local oxygenation and metabolic regulatory mechanisms. In the field of tissue engineering, we observe that D-DAM, with its higher content of neural and vascular components, is less conducive to fat regeneration. Previous reports using mixed layers of SAT from the abdominal and thigh also presented the unsatisfied adipogenesis property of vascular smooth muscle and neuron components [69]. Future investigations could explore methods to separate and remove these components to enhance the adipogenic efficacy of the bioscaffold.

The exact definition of ECM does not include cell components. Nevertheless, various decellularization methods can only remove cells with complete structure and genetic material such as DNA released after cell fragmentation. It is still challenging to completely remove all cellular debris, especially using the enzyme-free method. The remaining cell fragment proteins can be detected by highly sensitive proteomics and other assays and have been shown not to affect the biocompatibility and immunogenicity of scaffolds [70]. We analyzed the intracellular protein components identified within the DAM and revealed notably higher levels of mitochondria-related proteins in S-DAM, whereas D-DAM contained elevated amounts of proteins involved in mRNA processing and endocrine pathways. Further Protein-Protein Interaction (PPI) analysis pinpointed the most densely interconnected proteins including HNRNPA2B1, HNRNPA1, and HNRNPC. In light of this finding, and considering prior research indicating weaker multilineage differentiation potential of ADSC from dSAT [38], we postulate that adipocytes in dSAT may exhibit a more refined or active gene expression regulation, with the cells existing in a more specialized differentiation state necessitating increased mRNA processing to maintain their specific cellular functions, such as lipid metabolism and endocrine activity. This would enable a more adaptive response to environmental stimuli, including mechanical stress, metabolic stress, and hormonal fluctuations [67]. Conversely, the higher mitochondrial-associated proteins in S-DAM imply a potentially greater efficiency in energy production and utilization, a metabolic advantage that may translate into a more favorable environment retained in the ECM post-decellularization. However, it has been reported that mitochondria are present in DAM with poorer adipogenic potential [71]. The direct relationship between mitochondrial proteins and the adipogenic ability of DAM still requires further investigation. The heightened levels of cytokines, growth factors, and chemokines detected in S-DAM in our study align with this conjecture, as cytokines are known to effectively promote homing, proliferation, and differentiation of adipocyte precursor cells [72]. These findings suggest a potential direct link between metabolic status and regenerative property, suggesting novel avenues for enhancing tissue regenerative capabilities through metabolic pathway modulation.

Multiple decellularization methods have been reported in the literature. Our preliminary research indicated that the enzyme-free method exhibits higher decellularization efficiency and superior lipogenic effects compared to the classic method invented by Flynn [2,70]. Furthermore, by eliminating the use of enzymes, this approach also offers enhancements in terms of cost-effectiveness and biosafety. Consequently, the enzyme-free decellularization method was employed in this study. A comprehensive assessment of the long-term impacts of ECM on adipocyte behavior and overall metabolic homeostasis will advance our understanding of adipose tissue biology and lead to breakthroughs for the prevention and treatment of metabolic diseases [73]. For instance, therapies targeting neuromodulation or angiogenesis in dSAT. Notably, as a preliminary study, our study was confined to individuals with normal BMI and healthy physical conditions. Future endeavors should encompass a broader range of donors, including those with obesity and diabetes, to elucidate the specific molecular mechanisms underlying the interactions between the nervous and vascular systems and adipocytes in deep fat depots. Furthermore, recent literature has highlighted a communication mechanism between ECM and mitochondria-mediated by TMEM2 signaling, implicating links with immune pathways [69]. This suggests a complex interplay between mitochondria and ECM that warrants further investigation. Given the enhanced mitochondrial content in S-DAM and its superior potential for fat regeneration, there is a need to further delineate the precise role of mitochondria in the adipogenesis process. By selecting the source of the scaffold and eliminating components useless to regeneration, the functional capacity of the scaffold can be enhanced, thereby facilitating personalized, high-efficiency strategies for soft tissue reconstruction.

5. Conclusions

In this study, we elucidated the distinct physical-mechanical properties and compositional differences of the ECM derived from superficial and deep abdominal subcutaneous fat, which serves as the main donor of DAM. DAM from the Superficial layer exhibits a superior capacity for fat regeneration compared to the deep layer. The enrichment of neural, vascular, and mRNA processing proteins in D-DAM suggests an adverse impact on adipogenesis. The higher mitochondrial content of S-DAM, which presents as a more promising candidate for regenerative medicine, suggests a potential direct correlation between metabolic status and regenerative properties. These findings not only deepen our comprehension of the impact of donor characteristics on the property of adipogenesis bioscaffold but also introduce innovative perspectives and

potential applications in regenerative medicine.

CRediT authorship contribution statement

Xiaomu Ma: Writing – original draft, Formal analysis, Data curation, Conceptualization. **Qiang Yue:** Methodology, Formal analysis, Data curation, Conceptualization, Writing – original draft. **Su Fu:** Methodology, Supervision. **Chunjun Liu:** Methodology, Resources, Supervision. **Jie Luan:** Writing – review & editing, Funding acquisition, Project administration.

Declaration of competing interest

The authors declare that they have no known competing financial interests or personal relationships that could have appeared to influence the work reported in this paper.

Data availability

Data will be made available on request.

Acknowledgements

This study was founded by National Key Clinical Specialty Discipline Construction Program of China (1112621048). None of the authors has a financial interest to declare in relation to the content of this article.

References

[1] B.R. Freedman, D.J. Mooney, Biomaterials to mimic and heal connective tissues, Adv Mater 31 (2019) e1806695, https://doi.org/10.1002/adma.201806695.
[2] L.E. Flynn, The use of decellularized adipose tissue to provide an inductive microenvironment for the adipogenic differentiation of human adipose-derived stem cells, Biomaterials 31 (2010) 4715–4724, https://doi.org/10.1016/j.biomaterials.2010.02.046.
[3] A.E. Turner, C. Yu, J. Bianco, et al., The performance of decellularized adipose tissue microcarriers as an inductive substrate for human adipose-derived stem cells, Biomaterials 33 (2012) 4490–4499, https://doi.org/10.1016/j.biomaterials.2012.03.026.
[4] V. Liakouli, P. Cipriani, P. Di Benedetto, et al., The role of extracellular matrix components in angiogenesis and fibrosis: possible implication for Systemic Sclerosis, Mod. Rheumatol. 28 (2018) 922–932, https://doi.org/10.1080/14397595.2018.1431004.
[5] S. Kumari, P. Singh, R. Singh, Repeated Silica exposures lead to Silicosis severity via PINK1/PARKIN mediated mitochondrial dysfunction in mice model, Cell. Signal. 121 (2024) 111272, https://doi.org/10.1016/j.cellsig.2024.111272.
[6] M. Roth, B. Han, T. S'Ng C, et al., Zinc iodide dimethyl sulfoxide reduces collagen deposition by increased matrix metalloproteinase-2 expression and activity in lung fibroblasts, Biomedicines 12 (2024), https://doi.org/10.3390/biomedicines12061257.
[7] I.C. Wilkie, Basement membranes, brittlestar tendons, and their mechanical adaptability, Biology 13 (2024), https://doi.org/10.3390/biology13060375.
[8] S.J. Conner, H.B. Borges, J.R. Guarin, et al., Obesity Induces Temporally Regulated Alterations in the extracellular matrix that drive breast tumor invasion and metastasis, Cancer Res. (2024), https://doi.org/10.1158/0008-5472.Can-23-2526.
[9] P. Sawadkar, N. Mandakhbayar, K.D. Patel, et al., Three dimensional porous scaffolds derived from collagen, elastin and fibrin proteins orchestrate adipose tissue regeneration, J. Tissue Eng. 12 (2021) 20417314211019238, https://doi.org/10.1177/20417314211019238.
[10] P. Sawadkar, N. Mandakhbayar, K.D. Patel, et al., 3D porous binary composites of collagen, elastin, and fibrin proteins orchestrate adipose tissue regeneration, Macromol. Biosci. 24 (2024) e2400073, https://doi.org/10.1002/mabi.202400073.
[11] Z. Zhou, J. Cui, S. Wu, et al., Silk fibroin-based biomaterials for cartilage/osteochondral repair, Theranostics 12 (2022) 5103–5124, https://doi.org/10.7150/thno.74548.
[12] T. Krieg, M. Aumailley, The extracellular matrix of the dermis: flexible structures with dynamic functions, Exp. Dermatol. 20 (2011) 689–695, https://doi.org/10.1111/j.1600-0625.2011.01313.x.
[13] P. Sompunga, W. Rodprasert, S. Srisuwatanasagul, et al., Preparation of decellularized tissue as dual cell carrier systems: a step towards facilitating Re-epithelization and cell encapsulation for tracheal reconstruction, Ann. Biomed. Eng. 52 (2024) 1222–1239, https://doi.org/10.1007/s10439-024-03448-6.
[14] T. Karkhanis, A.G. Byju, D.L. Morales, et al., Composite biosynthetic graft for repair of long-segment tracheal stenosis: a pilot in vivo and in vitro feasibility study, ASAIO journal (American Society for Artificial Internal Organs 70 (1992) 527–534, https://doi.org/10.1097/mat.0000000000002130.
[15] I. Klabukov, D. Atiakshin, E. Kogan, et al., Post-implantation inflammatory responses to xenogeneic tissue-engineered cartilage implanted in rabbit trachea: the role of cultured chondrocytes in the modification of inflammation, Int. J. Mol. Sci. 24 (2023), https://doi.org/10.3390/ijms242316783.
[16] H.H. Shin, J. Park, Y.J. Kim, et al., Hydrophilic/hydrophobic janus nanofibers containing compound K for cartilage regeneration, International journal of nanomedicine 19 (2024) 1683–1697, https://doi.org/10.2147/ijn.S435156.
[17] M.M. Joglekar, N.J. Bekker, M.L. Koloko Ngassie, et al., The lung extracellular matrix protein landscape in severe early-onset and moderate chronic obstructive pulmonary disease, Am. J. Physiol. Lung Cell Mol. Physiol. (2024), https://doi.org/10.1152/ajplung.00332.2023.
[18] K. Devi, M.S. Tomar, M. Barsain, et al., Regeneration capability of neonatal lung-derived decellularized extracellular matrix in an emphysema model, J. Contr. Release : official journal of the Controlled Release Society 372 (2024) 234–250, https://doi.org/10.1016/j.jconrel.2024.05.043.
[19] A. Ulldemolins, M. Narciso, H. Sanz-Fraile, et al., Effects of aging on the biomechanical properties of the lung extracellular matrix: dependence on tissular stretch, Front. Cell Dev. Biol. 12 (2024) 1381470, https://doi.org/10.3389/fcell.2024.1381470.
[20] R. Quinteira, S. Gimondi, N.O. Monteiro, et al., Decellularized kidney extracellular matrix-based hydrogels for renal tissue engineering, Acta Biomater. 180 (2024) 295–307, https://doi.org/10.1016/j.actbio.2024.04.026.
[21] U. Rende, S.B. Ahn, S. Adhikari, et al., Deciphering the kidney matrisome: identification and quantification of renal extracellular matrix proteins in healthy mice, Int. J. Mol. Sci. 24 (2023), https://doi.org/10.3390/ijms24032827.
[22] C.M. Kerr, S.E. Silver, Y.S. Choi, et al., Decellularized heart extracellular matrix alleviates activation of hiPSC-derived cardiac fibroblasts, Bioact. Mater. 31 (2024) 463–474, https://doi.org/10.1016/j.bioactmat.2023.08.023.
[23] K.C. Kiliç, Y. Yazir, A. Öztürk, et al., Investigation of impacts of decellularized heart extracellular matrix and VEGF on cardiomyogenic differentiation of mesenchymal stem cell through Notch/Hedgehog signaling pathways, Tissue Cell 84 (2023) 102195, https://doi.org/10.1016/j.tice.2023.102195.
[24] T.T. Han, S. Toutounji, B.G. Amsden, et al., Adipose-derived stromal cells mediate in vivo adipogenesis, angiogenesis and inflammation in decellularized adipose tissue bioscaffolds, Biomaterials 72 (2015) 125–137, https://doi.org/10.1016/j.biomaterials.2015.08.053.
[25] J. Feng, S. Fu, J. Luan, Harnessing fine fibers in decellularized adipose-derived matrix for enhanced adipose regeneration, Mater Today Bio 25 (2024) 100974, https://doi.org/10.1016/j.mtbio.2024.100974.
[26] J. Yang, J. Tang, J. Dang, et al., Bioactive decellularized adipose matrix prepared using a rapid, nonchemical/enzymatic method for adipogenesis, Biotechnol. Bioeng. 121 (2024) 157–175, https://doi.org/10.1002/bit.28547.
[27] M.E. Ziegler, K. Khabaz, N. Khoshab, et al., Combining allograft adipose and fascia matrix as an off-the-shelf scaffold for adipose tissue engineering stimulates angiogenic responses and activates a proregenerative macrophage profile in a rodent model, Ann. Plast. Surg. 91 (2023) 294–300, https://doi.org/10.1097/sap.0000000000003587.
[28] M. Xu, Y. He, Y. Li, et al., Combined use of autologous sustained-release scaffold of adipokines and acellular adipose matrix to construct vascularized adipose tissue, Plast. Reconstr. Surg. 153 (2024) 348e–350e, https://doi.org/10.1097/prs.0000000000010649.
[29] K. Seretis, D.G. Goulis, G. Koliakos, et al., The effects of abdominal lipectomy in metabolic syndrome components and insulin sensitivity in females: a systematic review and meta-analysis, Metab., Clin. Exp. 64 (2015) 1640–1649, https://doi.org/10.1016/j.metabol.2015.09.015.
[30] M. Lin, J. Ge, X. Wang, et al., Biochemical and biomechanical comparisions of decellularized scaffolds derived from porcine subcutaneous and visceral adipose tissue, J. Tissue Eng. 10 (2019) 2041731419888168, https://doi.org/10.1177/2041731419888168.
[31] F. Louwen, A. Ritter, N.N. Kreis, et al., Insight into the development of obesity: functional alterations of adipose-derived mesenchymal stem cells, Obes. Rev. : an official journal of the International Association for the Study of Obesity 19 (2018) 888–904, https://doi.org/10.1111/obr.12679.
[32] K.S. Vyas, M. Bole, H.C. Vasconez, et al., Profile of adipose-derived stem cells in obese and lean environments, Aesthetic Plast. Surg. 43 (2019) 1635–1645, https://doi.org/10.1007/s00266-019-01397-3.
[33] R. Joshi, H. Duong, Anatomy, Abdomen and Pelvis, Scarpa Fascia [M]. StatPearls. Treasure Island (FL); StatPearls Publishing Copyright © 2022, StatPearls Publishing LLC, 2022.
[34] T.H. Le Jemtel, R. Samson, G. Milligan, et al., Visceral adipose tissue accumulation and residual cardiovascular risk, Curr. Hypertens. Rep. 20 (2018) 77, https://doi.org/10.1007/s11906-018-0880-0.
[35] L. Liu, J. Feng, G. Zhang, et al., Visceral adipose tissue is more strongly associated with insulin resistance than subcutaneous adipose tissue in Chinese subjects with pre-diabetes, Curr. Med. Res. Opin. 34 (2018) 123–129, https://doi.org/10.1080/03007995.2017.1364226.
[36] G. Di Taranto, C. Cicione, G. Visconti, et al., Qualitative and quantitative differences of adipose-derived stromal cells from superficial and deep subcutaneous lipoaspirates: a matter of fat, Cytotherapy 17 (2015) 1076–1089, https://doi.org/10.1016/j.jcyt.2015.04.004.
[37] G. Cappellano, E.M. Morandi, J. Rainer, et al., Human macrophages preferentially infiltrate the superficial adipose tissue, Int. J. Mol. Sci. 19 (2018), https://doi.org/10.3390/ijms19051404.
[38] B.M. Schipper, K.G. Marra, W. Zhang, et al., Regional anatomic and age effects on cell function of human adipose-derived stem cells, Ann. Plast. Surg. 60 (2008) 538–544, https://doi.org/10.1097/SAP.0b013e3181723bbe.

[39] A. Ferguson, L. Wang, R.B. Altman, et al., Functional dynamics within the human ribosome regulate the rate of active protein synthesis, Mol Cell 60 (2015) 475–486, https://doi.org/10.1016/j.molcel.2015.09.013.
[40] M.P. Paronetto, T. Achsel, A. Massiello, et al., The RNA-binding protein Sam68 modulates the alternative splicing of Bcl-x, J. Cell Biol. 176 (2007) 929–939, https://doi.org/10.1083/jcb.200701005.
[41] C.J. David, M. Chen, M. Assanah, et al., HnRNP proteins controlled by c-Myc deregulate pyruvate kinase mRNA splicing in cancer, Nature 463 (2010) 364–368, https://doi.org/10.1038/nature08697.
[42] T. Treiber, N. Treiber, U. Plessmann, et al., A compendium of RNA-binding proteins that regulate MicroRNA biogenesis, Mol Cell 66 (2017) 270–275, https://doi.org/10.1016/j.molcel.2017.03.014.
[43] M.L. Li, J.Y. Lin, B.S. Chen, et al., EV71 3C protease induces apoptosis by cleavage of hnRNP A1 to promote apaf-1 translation, PLoS One 14 (2019) e0221048, https://doi.org/10.1371/journal.pone.0221048.
[44] J.H. Kim, K.Y. Paek, K. Choi, et al., Heterogeneous nuclear ribonucleoprotein C modulates translation of c-myc mRNA in a cell cycle phase-dependent manner, Mol. Cell Biol. 23 (2003) 708–720, https://doi.org/10.1128/mcb.23.2.708-720.2003.
[45] S. Shetty, Regulation of urokinase receptor mRNA stability by hnRNP C in lung epithelial cells, Mol. Cell. Biochem. 272 (2005) 107–118, https://doi.org/10.1007/s11010-005-7644-2.
[46] N. Liu, Q. Dai, G. Zheng, et al., N(6)-methyladenosine-dependent RNA structural switches regulate RNA-protein interactions, Nature 518 (2015) 560–564, https://doi.org/10.1038/nature14234.
[47] X. Wang, Q. Yang, X. Zhou, et al., Suppression of eEF2 phosphorylation alleviates synaptic failure and cognitive deficits in mouse models of Down syndrome, Alzheimers Dement (2024), https://doi.org/10.1002/alz.13916.
[48] X. Zhang, L. Han, J. Hou, et al., Stress granule-localized USP8 potentiates cGAS-mediated type I interferonopathies through deubiquitination of DDX3X, Cell Rep. 43 (2024) 114248, https://doi.org/10.1016/j.celrep.2024.114248.
[49] S.H. Kim, J. Turnbull, S. Guimond, Extracellular matrix and cell signalling: the dynamic cooperation of integrin, proteoglycan and growth factor receptor, J. Endocrinol. 209 (2011) 139–151, https://doi.org/10.1530/joe-10-0377.
[50] B.P. Tewari, K. Conant, Editorial: emerging roles of extracellular matrix in the physiology and pathophysiology of the central nervous system, Front. Cell. Neurosci. 18 (2024) 1400652, https://doi.org/10.3389/fncel.2024.1400652.
[51] M. Votteler, P.J. Kluger, H. Walles, et al., Stem cell microenvironments–unveiling the secret of how stem cell fate is defined, Macromol. Biosci. 10 (2010) 1302–1315, https://doi.org/10.1002/mabi.201000102.
[52] S. Khetan, M. Guvendiren, W.R. Legant, et al., Degradation-mediated cellular traction directs stem cell fate in covalently crosslinked three-dimensional hydrogels, Nat. Mater. 12 (2013) 458–465, https://doi.org/10.1038/nmat3586.
[53] K.A. Kilian, B. Bugarija, B.T. Lahn, et al., Geometric cues for directing the differentiation of mesenchymal stem cells, Proc. Natl. Acad. Sci. U.S.A. 107 (2010) 4872–4877, https://doi.org/10.1073/pnas.0903269107.
[54] J. Lee, A.A. Abdeen, D. Zhang, et al., Directing stem cell fate on hydrogel substrates by controlling cell geometry, matrix mechanics and adhesion ligand composition, Biomaterials 34 (2013) 8140–8148, https://doi.org/10.1016/j.biomaterials.2013.07.074.
[55] R. McBeath, D.M. Pirone, C.M. Nelson, et al., Cell shape, cytoskeletal tension, and RhoA regulate stem cell lineage commitment, Dev. Cell 6 (2004) 483–495, https://doi.org/10.1016/s1534-5807(04)00075-9.
[56] J.K. Kular, S. Basu, R.I. Sharma, The extracellular matrix: structure, composition, age-related differences, tools for analysis and applications for tissue engineering, J. Tissue Eng. 5 (2014) 2041731414557112, https://doi.org/10.1177/2041731414557112.
[57] M. Koenen, M.A. Hill, P. Cohen, et al., Obesity, adipose tissue and vascular dysfunction, Circ. Res. 128 (2021) 951–968, https://doi.org/10.1161/circresaha.121.318093.
[58] J. Eyckmans, T. Boudou, X. Yu, et al., A hitchhiker's guide to mechanobiology, Dev. Cell 21 (2011) 35–47, https://doi.org/10.1016/j.devcel.2011.06.015.
[59] E.M. Janse, S.H. Jeurissen, Ontogeny and function of two non-lymphoid cell populations in the chicken embryo, Immunobiology 182 (1991) 472–481, https://doi.org/10.1016/s0171-2985(11)80211-1.
[60] A. Kayabolen, D. Keskin, A. Aykan, et al., Native extracellular matrix/fibroin hydrogels for adipose tissue engineering with enhanced vascularization, Biomedical materials (Bristol, England) 12 (2017) 035007, https://doi.org/10.1088/1748-605X/aa6a63.
[61] T. Watchararot, W. Prasongchean, P. Thongnuek, Angiogenic property of silk fibroin scaffolds with adipose-derived stem cells on chick chorioallantoic membrane, R. Soc. Open Sci. 8 (2021) 201618, https://doi.org/10.1098/rsos.201618.
[62] C. Jean, P. Gravelle, J.J. Fournie, et al., Influence of stress on extracellular matrix and integrin biology, Oncogene 30 (2011) 2697–2706, https://doi.org/10.1038/onc.2011.27.
[63] S. Gobaa, S. Hoehnel, M. Roccio, et al., Artificial niche microarrays for probing single stem cell fate in high throughput, Nat. Methods 8 (2011) 949–955, https://doi.org/10.1038/nmeth.1732.
[64] E.M. Chandler, C.M. Berglund, J.S. Lee, et al., Stiffness of photocrosslinked RGD-alginate gels regulates adipose progenitor cell behavior, Biotechnol. Bioeng. 108 (2011) 1683–1692, https://doi.org/10.1002/bit.23079.
[65] D.A. Young, Y.S. Choi, A.J. Engler, et al., Stimulation of adipogenesis of adult adipose-derived stem cells using substrates that mimic the stiffness of adipose tissue, Biomaterials 34 (2013) 8581–8588, https://doi.org/10.1016/j.biomaterials.2013.07.103.
[66] J.M. Sobral, S.G. Caridade, R.A. Sousa, et al., Three-dimensional plotted scaffolds with controlled pore size gradients: effect of scaffold geometry on mechanical performance and cell seeding efficiency, Acta Biomater. 7 (2011) 1009–1018, https://doi.org/10.1016/j.actbio.2010.11.003.
[67] B. Gondal, Body Contouring: Art, Science, and Clinical Practice, 2010.
[68] C. Stecco, R. Schleip, A fascia and the fascial system, J. Bodyw. Mov. Ther. 20 (2016) 139–140, https://doi.org/10.1016/j.jbmt.2015.11.012.
[69] H. Zhang, C.K. Tsui, G. Garcia, et al., The extracellular matrix integrates mitochondrial homeostasis, Cell (2024), https://doi.org/10.1016/j.cell.2024.05.057.
[70] J. Qi, Z. Li, S. Li, et al., Effectiveness of a new enzyme-free method for the preparation of a decellularized adipose-derived matrix, Aesthetic Surg. J. 44 (2024) Np184–np186, https://doi.org/10.1093/asj/sjad307.
[71] X. Ma, Q. Yue, Q. Wang, et al., Hydrophilic components as Key active ingredients in adipose-derived matrix bioscaffolds for inducing fat regeneration, Adv. Healthcare Mater. (2024) e2402331, https://doi.org/10.1002/adhm.202402331.
[72] Y. Chen, Y. Li, B. Li, et al., Migrasomes from adipose derived stem cells enrich CXCL12 to recruit stem cells via CXCR4/RhoA for a positive feedback loop mediating soft tissue regeneration, J. Nanobiotechnol. 22 (2024) 219, https://doi.org/10.1186/s12951-024-02482-9.
[73] K. Hamsho, M. Broadwin, C.R. Stone, et al., The current state of extracellular matrix therapy for ischemic heart disease, Med. Sci. 12 (2024), https://doi.org/10.3390/medsci12010008.